Stabilizing Effect of Magnetic Helicity on Magnetic Cavities in the Intergalactic Medium

Candelaresi, Simon; Sordo, Fabio Del

Published in:
Astrophysical Journal

DOI:
10.3847/1538-4357/ab8dc0

Publication date:
2020

The Astrophysical Journal, 896:86 (9pp), 2020 June 10 https://doi.org/10.3847/1538-4357/ab8dc0

Stabilizing Effect of Magnetic Helicity on Magnetic Cavities in the Intergalactic Medium

Simon Candelaresi[1,2] and Fabio Del Sordo[3,4]
[1] School of Mathematics and Statistics, University of Glasgow, Glasgow G12 8QQ, UK; simon.candelaresi@gmail.com
[2] Division of Mathematics, University of Dundee, Dundee DD1 4HN, UK
[3] Institute of Astrophysics, FORTH, GR-71110 Heraklion, Greece
[4] Department of Physics, University of Crete, GR-70013 Heraklion, Greece; fabiods@ia.forth.gr
Received 2019 December 27; revised 2020 April 14; accepted 2020 April 26; published 2020 June 16

Abstract

We investigate the effect of magnetic helicity on the stability of buoyant magnetic cavities as found in the intergalactic medium. In these cavities we insert helical magnetic fields and test whether or not helicity can increase their stability to shredding through the Kelvin–Helmholtz instability and, with that, their lifetime. This is compared to the case of an external vertical magnetic field that is known to reduce the growth rate of the Kelvin–Helmholtz instability. By comparing a low-helicity configuration with a high-helicity one with the same magnetic energy, we find that an internal helical magnetic field stabilizes the cavity. This effect increases as we increase the helicity content. Stabilizing the cavity with an external magnetic field requires instead a significantly stronger field at higher magnetic energy. We conclude that the presence of helical magnetic fields is a viable mechanism to explain the stability of intergalactic cavities on timescales longer than 100 Myr.

Unified Astronomy Thesaurus concepts: Warm-hot intergalactic medium (1786); Magnetic fields (994)

1. Introduction

Intergalactic hot cavities have been observed to emanate from galactic disks in clusters of galaxies (e.g., Carilli et al. 1994; Churazov et al. 2001; Carilli & Taylor 2002; Taylor et al. 2002; Bîrzan et al. 2004; McNamara & Nulsen 2007; Montmerle 2011). Similar but different structures have also been observed around our Galaxy, Fermi Bubbles (Su et al. 2010), and their formation mechanism is still elusive (Yang et al. 2018). Observations seem to indicate that such intergalactic structures form as consequences of radio jets emanated by supermassive black holes or by active galactic nuclei (AGN) and their interaction with extragalactic plasma. These AGN-inflated radio bubbles in the intergalactic medium are seen in X-ray images of galaxy clusters. A shock is produced as the jet penetrates the surrounding medium, and in order to achieve pressure equilibrium, the jet material expands, leading to the formation of a low-density cavity. Bubbles at 10 kpc from the galactic center are found to be at least a factor of 3 less dense than the surrounding medium.

These hot cavities propagate through the intergalactic medium, where they are subject to magnetohydrodynamical instabilities, such as the Rayleigh-Taylor instability, the Richtmyer-Meshkov instability, and in particular the Kelvin–Helmholtz (KH) instability, after which turbulent mixing occurs. However, estimates of their lifetimes using their terminal velocity (e.g., Bîrzan et al. 2004) suggest that they survive significantly longer than they should (of the order of 10–100 Myr).

The intergalactic medium can be modeled as high-conductivity plasma. Chandrasekhar (1961) and Sharma & Srivastava (1968) showed analytically how in the presence of a magnetic field parallel to the velocity, the KH instability is suppressed. However, a perpendicular field has no effect on the growth of the modes. The effect of an external magnetic field on the stability of the cavities has been the subject of several studies (e.g., Robinson et al. 2004). However, the interiors of these cavities may be magnetized too. This is possible, for instance, if the jet responsible for their inflation is magnetized. Also, there is the possibility that the turbulent motions arising during the generation of the cavities may amplify the magnetic field in its interior through, e.g., a dynamo effect. The hypothesis of a helical magnetic field lying inside these bubbles appears justified, in light of results showing that AGN jets are characterized by helical magnetic fields (Li et al. 2006; Tang 2008; Gabuzda 2018). If this field contains magnetic helicity, it is stable on diffusive times, i.e., the energy and topology change insignificantly during this period (e.g., Del Sordo et al. 2010; Candelaresi & Brandenburg 2011).

If such an internal field was not stretched throughout the cavity boundaries where the KH instability occurs, it would have no immediate effect on the instability and we would not see a direct suppression of it. However, as the instability grows and leaves the linear regime, it can potentially be suppressed at this later stage.

Intergalactic cavities have been simulated in the past and different effects were considered in order to understand their evolution and stability. For instance, Brüggen (2003) studied the cooling behavior in buoyant bubbles in galactic clusters, where there is a significant growth of the KH instability. The inflation process of the bubble also plays a role in determining the bubble's stability. Pizzolato & Soker (2006) illustrated how the initial deceleration and drag, albeit unable to prevent the disruption of a bubble, may significantly lengthen a cavity's lifetime, and Sternberg & Soker (2008) proposed such dynamics as the explanation for why long-lasting cavities exist. Braithwaite (2010) studied the magnetohydrodynamic relaxation of AGN ejecta, finding that the timescale on which the bubble reaches an equilibrium depends on the magnetization and the helicity of the outflow. It should be noted, however, that this study did not include the effect of buoyancy. Subsequently, Gourgouliatos et al. (2010) studied the problem with both analytical and numerical approaches, finding that the presence of both poloidal and toroidal components of the

magnetic field in intergalactic cavities does indeed induce stability. Liu et al. (2008) showed how the ratio of the toroidal to poloidal magnetic field of the bubble determines the direction of bubble expansion and propagation, which can develop asymmetries about its propagation axis. Dong & Stone (2009) studied the effect of magnetic fields and anisotropic viscosity, finding that a critical role for the evolution of the bubble is played by the initial field geometry, and that toroidal field loops initially located inside the bubble are the best option to reproduce the observed cavity structures.

Vogt & Enßlin (2005) observed how the typical length scale of magnetic fields in the Hydra A cluster is smaller than the typical bubble size, and concluded that the scenario of an uniform external field is not supported. Based on this result Ruszkowski et al. (2007) studied the effect of a random magnetic field, taking into account both the helical and non-helical cases. They argued that when the gas pressure is higher than the magnetic pressure, that is, for high plasma β ($\sim$40 in their case), a random helical magnetic field cannot stabilize the bubble. Still, they could not exclude that stabilization is taking place if plasma β is locally lower inside the intergalactic cavities. In contrast, Jones & De Young (2005) found with 2D simulations that microGauss magnetic fields can stabilize these bubbles. In general, the evolution of the helicity of extra-galactic bubbles and its interaction with the intergalactic medium, after the bubble's inflation and detachment from the jet, have been only marginally studied and they are not yet well understood, especially in three dimensions. Therefore, further investigation is needed, and the research we present intends to be a step in this direction.

The aim of this work is to investigate the stabilizing effects of internal helical magnetic fields on the intergalactic cavities where they may be harbored. Moreover, we aim to compare their stabilizing effect to that of a homogeneous external vertical field to evaluate whether a similar stabilizing effect may be attained with weaker fields. This work is organized as follows. In Section 2 we illustrate the model we implemented. In Section 3 we discuss the effect of an internal helical magnetic field for two different kinds of initial magnetic field. In Section 4 we show the effect of an external magnetic field. In Section 5 we draw conclusions and discuss the implications of this work.

2. Model

Our model setup consists of a hot under-dense bubble embedded in a stably stratified medium with gravity. This bubble rises through buoyancy, which leads to shear with the surrounding stationary medium and the onset of the Kelvin–Helmholtz instability on the bubble's surface. Our goal is to study how the stability of the bubble depends on the presence of magnetic fields. Therefore, concerning the stability of the bubbles we will consider four cases: (i) a purely hydrodynamical case, (ii) an internal ABC helical magnetic field, (iii) an internal spheromak magnetic field, and (iv) an external vertical magnetic field. The last scenario has already been studied for the Kelvin–Helmholtz instability for incompressible and compressible media by Chandrasekhar (1961) and here we will use it as a reference. Cases (ii) and (iii) will be further subdivided into a high-helicity and low-helicity cases, while for case (iv) we will take into account strong and weak external-field cases.

2.1. Governing Equations

To approach this problem and to provide a quantitative assessment we make use of direct numerical simulations, which we perform with the public code PENCILCODE.[5] This code is particularly suitable for our study since it avoids using the magnetic field $\boldsymbol{B}$ as a primary variable and instead uses its vector potential $\boldsymbol{A}$, ensuring the fields stay solenoidal throughout the simulations. Moreover, it allows us to quantify the magnetic helicity $H = \int \boldsymbol{A} \cdot \boldsymbol{B} \mathrm{d}V$, where the integral is calculated over the whole computational domain. For our study we require an ideally conducting viscous medium. This is governed by the resistive magnetohydrodynamics equation together with the energy (temperature) equation:

$$\frac{\partial \boldsymbol{A}}{\partial t} = \boldsymbol{u} \times \boldsymbol{B} + \eta \boldsymbol{\nabla}^2 \boldsymbol{A}, \tag{1}$$

$$\frac{\mathrm{D}\boldsymbol{u}}{\mathrm{D}t} = -c_\mathrm{s}^2 \boldsymbol{\nabla}\left(\frac{\ln T}{\gamma} + \ln \rho\right) + \frac{\boldsymbol{J} \times \boldsymbol{B}}{\rho} - \boldsymbol{g} + \boldsymbol{F}_\mathrm{visc}, \tag{2}$$

$$\frac{\mathrm{D}\ln\rho}{\mathrm{D}t} = -\boldsymbol{\nabla} \cdot \boldsymbol{u}, \tag{3}$$

$$\frac{\partial \ln T}{\partial t} = -\boldsymbol{u} \cdot \boldsymbol{\nabla} \ln T - (\gamma - 1)\boldsymbol{\nabla} \cdot \boldsymbol{u} + \frac{1}{\rho c_v T}(\boldsymbol{\nabla} \cdot (K \boldsymbol{\nabla} T) + \eta \boldsymbol{J}^2 + 2\rho\nu \mathbf{S} \otimes \mathbf{S} + \zeta\rho(\boldsymbol{\nabla} \cdot \boldsymbol{u})^2), \tag{4}$$

with the magnetic vector potential $\boldsymbol{A}$, magnetic field $\boldsymbol{B} = \boldsymbol{\nabla} \times \boldsymbol{A}$, fluid velocity $\boldsymbol{u}$, constant magnetic resistivity (diffusivity) η, advective derivative $\mathrm{D}/\mathrm{D}t = \partial/\partial t + \boldsymbol{u} \cdot \boldsymbol{\nabla}$, sound speed $c_\mathrm{s} = \gamma p/\rho$, adiabatic index $\gamma = c_p/c_v$, heat capacities c_p and c_v at constant pressure and volume, temperature T, density ρ, electric current density $\boldsymbol{J} = \boldsymbol{\nabla} \times \boldsymbol{B}$, gravitational acceleration $\boldsymbol{g}$, viscous force $\boldsymbol{F}_\mathrm{visc}$, heat conductivity K, and bulk viscosity ζ. The viscous force is given as $\boldsymbol{F}_\mathrm{visc} = \rho^{-1}\boldsymbol{\nabla} \cdot 2\nu\rho\mathbf{S}$, with the traceless rate of strain tensor $S_{ij} = \frac{1}{2}(u_{i,j} + u_{j,i}) - \frac{1}{3}\delta_{ij}\boldsymbol{\nabla} \cdot \boldsymbol{u}$. The equation of state used here is for the ideal monoatomic gas and it appears implicitly in our equations, as we eliminated pressure p. Here the gas is monatomic with $\gamma = 5/3$.

Our side boundaries (xy) are chosen to be periodic, while the bottom is closed ($\boldsymbol{u} \cdot \boldsymbol{n} = 0$) and the top open. This allows for outward fluxes. For the magnetic field the vertical boundaries are set to open, allowing magnetic flux.

As a simulation domain we choose a box of size 2.4×2.4 in the horizontal (xy) plane and 9.6 in the vertical (z), using $480 \times 480 \times 1920$ meshpoints.

In order to reduce resistive magnetic helicity decay we choose a value of the magnetic resistivity as low as the resolution allows. Here we set it to $\eta = 3 \times 10^{-4}$. Viscosity is either set to $\nu = 1 \times 10^{-3}$ or to $\nu = 2 \times 10^{-4}$ to check that the overall behavior of the simulation does not depend on this parameter, which prevents any accumulation of turbulent energy at small scales.

[5] https://github.com/pencil-code

With the viscosity and magnetic resistivity we can then compute our Reynolds numbers:

$$\mathrm{Re} = \frac{u_{\max} d}{\nu}, \tag{5}$$

$$\mathrm{Re_M} = \frac{u_{\max} d}{\eta}, \tag{6}$$

with the maximum velocity $u_{\max}$ and bubble diameter $d = 1.6$.

2.2. Initial Thermodynamic Conditions

As an initial condition we choose a stably stratified atmosphere in which we place an under-dense hot cavity of spherical shape. This can be found as part of the PENCILCODE under src/initial_condition/bubbles_init.f90. The stable atmosphere obeys the hydrostatic equilibrium

$$\rho g = -\nabla p, \tag{7}$$

with the gravitational acceleration in the negative z-direction g. Our model atmosphere extends in the z-direction, which makes the gradient a derivative in z and we can rewrite Equation (7) as

$$\rho g = -\frac{\mathrm{d}p}{\mathrm{d}z}. \tag{8}$$

Density, pressure, and temperature are related through the ideal gas law

$$p = \frac{R}{\mu}\rho T, \tag{9}$$

where μ is the mass of one mol of gas and $R = 8.31\ \mathrm{J\,K^{-1}\,mol^{-1}}$ is the ideal gas constant. With the ideal gas law we can express the hydrostatic equilibrium as

$$\frac{\mu g}{R}\frac{\mathrm{d}z}{T} = -\frac{\mathrm{d}p}{p}. \tag{10}$$

The gas is chosen to be adiabatic, i.e.,

$$p^{1-\gamma}T^{\gamma} = \mathrm{const.}, \tag{11}$$

which leads to the relation

$$\frac{\mathrm{d}p}{p} = \frac{\gamma}{\gamma - 1}\frac{\mathrm{d}T}{T}. \tag{12}$$

With Equation (10) we can write

$$\frac{\mathrm{d}T}{\mathrm{d}z} = -\frac{\gamma - 1}{\gamma}\frac{\mu g}{R}. \tag{13}$$

We now integrate this equation and obtain

$$T = -\frac{\gamma - 1}{\gamma}\frac{\mu g}{R}z + T_0, \tag{14}$$

where T_0 is the temperature at an arbitrary height z_0.

We now choose this height to be the isothermal scale height

$$z_0 = \frac{RT_0}{\mu g}. \tag{15}$$

This is justified if we assume that the gas is in isothermal equilibrium at z_0, which is a common assumption for the adiabatic atmosphere. Our temperature profile now obtains the form

$$T(z) = T_0\left(1 - \frac{\gamma - 1}{\gamma}\frac{z}{z_0}\right). \tag{16}$$

With the temperature profile and Equation (12) we can compute the pressure profile to

$$p(z) = p_0\left(1 - \frac{\gamma - 1}{\gamma}\frac{z}{z_0}\right)^{\gamma/(\gamma-1)}. \tag{17}$$

Taking Equation (8) we can also compute the density profile to

$$\rho(z) = \rho_0\left(1 - \frac{\gamma - 1}{\gamma}\frac{z}{z_0}\right)^{1/(\gamma-1)}. \tag{18}$$

For the cavity we choose a radius of 0.8 and place it centrally in x and y and at 0.8 in z. Its initial peak temperature is $T_{\mathrm{cavity}} = 4$ and density $\rho_{\mathrm{cavity}} = 0.25$. In order to avoid sudden wave formation we apply (sharp) smoothing for T_{cavity} and ρ_{cavity} near the edges using a tanh profile that matches the surrounding values. With that the temperature and density are constant up to ca. 72% of the radius of the cavity.

This should be contrasted with the surrounding medium, which is stably stratified with gravitational acceleration of $g = 0.1$. For that we choose $z_0 = 4$, $\rho_0 = 1$, and $T_0 = 1$ such that the cavity is in approximate pressure balance with its surrounding medium and its expansion or compression is insignificant.

2.3. Initial Magnetic Condition 1: ABC Field

For the simulations that include a magnetic field inside the bubble we consider two kinds of initial magnetic conditions. In the first case we insert a helical magnetic field of the Arnold–Beltrami–Childress (ABC) flow type:

$$\boldsymbol{A} = f(r)A_0\begin{pmatrix}\cos((y - y_{\mathrm{cavity}})k) + \sin((z - z_{\mathrm{cavity}})k)\\ \cos((z - z_{\mathrm{cavity}})k) + \sin((x - x_{\mathrm{cavity}})k)\\ \cos((x - x_{\mathrm{cavity}})k) + \sin((y - y_{\mathrm{cavity}})k)\end{pmatrix}, \tag{19}$$

with the function

$$f(r) = 1 - (r/r_{\mathrm{b}})^{n_{\mathrm{smooth}}} \tag{20}$$

that makes sure that the magnetic field vanishes outside the bubble without any strong current sheets. Here $r = \sqrt{(x - x_{\mathrm{cavity}})^2 + (y - y_{\mathrm{cavity}})^2 + (z - z_{\mathrm{cavity}})^2}$ and r_{b} is the radius of the bubble. We use as a smoothing coefficient $n_{\mathrm{smooth}} = 2$. For values of $r > r_{\mathrm{b}}$ we set the field to 0.

Taking the curl we obtain $\boldsymbol{B} = k\boldsymbol{A}$. The magnetic energy scales like $A_0^2k^2$, while the magnetic helicity scales like A_0^2k. By inversely scaling the amplitude A_0 and the inverse scale k we can change the magnetic helicity while keeping the magnetic energy fixed. For our low-helicity setup we choose $A_0 = 2.5 \times 10^{-2}$ and $k = 20$. For the high-helicity case we choose $A_0 = 0.1$ and $k = 5$. For simplicity we will occasionally write $H = 1$ and $H = 4$ for the two cases.

2.4. Initial Magnetic Condition 2: Spheromak Field

To make sure our results are not dependent on a specific initial geometry of the internal magnetic field, but only the topology described by the amount of magnetic helicity, we perform a second set of simulations that makes use of a

spheromak magnetic field. For that we use the form given by Aly & Amari (2012). There the magnetic field is given in spherical coordinates (r, θ, ϕ), with the origin at the bubble's center, as

$$\begin{aligned}\boldsymbol{B} = & 2A_0\frac{g(\alpha r)}{(\alpha r)^2}\cos(\theta)\hat{e}_r \\ & - A_0\frac{g'(\alpha r)}{\alpha r}\sin(\theta)\hat{e}_\theta \\ & + A_0\frac{g(\alpha r)}{\alpha r}\sin(\theta)\hat{e}_\phi,\end{aligned} \tag{21}$$

with $\alpha = \tau/r_\mathrm{b}$. The function g is given as

$$g(t) = \frac{t^2}{\tau^2} - \frac{3}{\tau\sin(t)}\left(\frac{\sin(t)}{t} - \cos(t)\right) \tag{22}$$

and its derivative is

$$g'(t) = \frac{2t}{\tau^2} - \frac{3}{\tau\sin(t)}\left(-\frac{\sin(t)}{t^2} + \frac{\cos(t)}{t} + \sin(t)\right), \tag{23}$$

with τ being the zeros of the equation $g(\tau) = 0$, which can be calculated numerically to $\tau_1 = 5.763$, $\tau_2 = 9.095$, $\tau_3 = 12.229$, $\tau_4 = 15.515$, and $\tau_5 = 18.689$ for the first five roots. We then perform the transformation into Cartesian coordinates using the relations

$$\begin{aligned}B_x = & B_r(x - x_\mathrm{cavity})/r \\ & + B_\theta(x - x_\mathrm{cavity})(z - z_\mathrm{cavity})/(r_{xy}r) \\ & - B_\phi(y - y_\mathrm{cavity})/r_{xy},\end{aligned} \tag{24}$$

$$\begin{aligned}B_y = & B_r(y - y_\mathrm{cavity})/r_\mathrm{b} \\ & + B_\theta(y - y_\mathrm{cavity})(z - z_\mathrm{cavity})/(r_{xy}r) \\ & + B_\phi(x - x_\mathrm{cavity})/r_{xy},\end{aligned} \tag{25}$$

$$B_z = B_r(z - z_\mathrm{cavity})/r_\mathrm{b} - B_\theta r_{xy}/r \tag{26}$$

with $r_{xy} = \sqrt{(x - x_\mathrm{cavity})^2 + (y - y_\mathrm{cavity})^2}$.

Aly & Amari (2012) derived this field for a cylindrically symmetric force balance between magnetic and pressure forces solving the Grad–Shafranov equation. However, we note that in our case the hydrostatic pressure is not constant in space. Nevertheless, since the pressure deviation from p_0 is of the order of 0.5% we assume it is constant in our bubble.

We restrict the field within the bubble by setting it to 0 outside. We can do this, as the field naturally and smoothly vanishes at $r = r_\mathrm{b}$ without generating any strong surface currents. To obtain the magnetic vector potential to this field we solve the equation $\boldsymbol{\nabla}^2\boldsymbol{A} = -\boldsymbol{\nabla}\times\boldsymbol{B}$ in Fourier space, where we use the Coulomb gauge ($\boldsymbol{\nabla}\cdot\boldsymbol{A} = 0$) and the fact that the field is periodic, since it vanishes at the boundaries. A rendering of the magnetic field can be seen in Figure 1.

2.5. Initial Magnetic Condition 3: Vertical Field

The third magnetic case we take into consideration is that of an initial vertical magnetic field

$$\boldsymbol{B} = B_0\boldsymbol{e}_z, \tag{27}$$

where B_0 is the initial amplitude of the field in the entire computational domain.

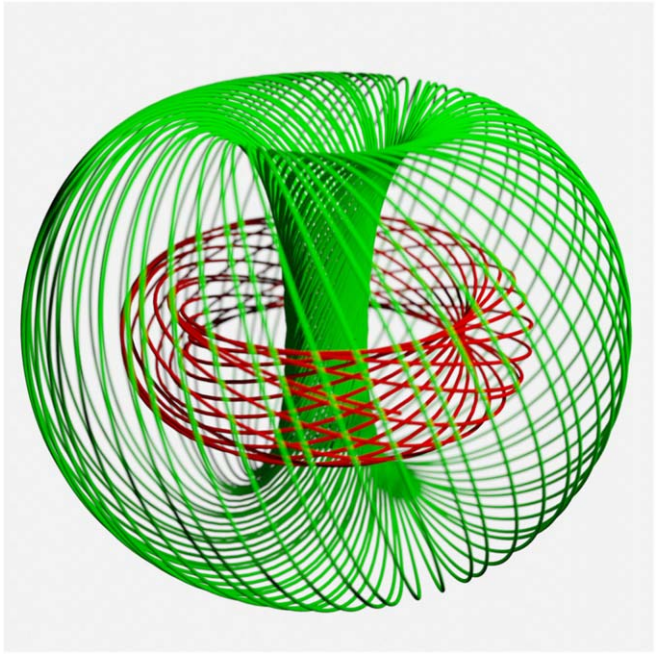

Figure 1. Rendering of two magnetic field lines for the spheromak initial condition.

2.6. Test Cases

For a fair comparison, and a quantitative evaluation of the role of magnetic fields in the three cases described in Sections 2.3, 2.4, and 2.5, we first perform calculations of a purely hydrodynamical case with no magnetic fields. We compare this with the two cases with an internal magnetic field within the cavities. The two ABC cases have almost the same magnetic energy of $E_\mathrm{m} = 0.2182$, while the two spheromak cases have energies of $E_\mathrm{m} = 0.264$ for the high-helicity and $E_\mathrm{m} = 0.189$ for the low-helicity case. This difference is a result of adjustments of the parameters that are chosen to match the magnetic helicity content of the ABC case as closely as possible, while keeping the difference with the magnetic energy minimal. Here the high-helicity case has a magnetic helicity content that is four times larger. An overview of the parameters used in the simulations is shown in Table 1. With these initial conditions we can compute the plasma β where the magnetic field is strongest using

$$\beta = \min\left(\frac{2(R\rho T/\mu)}{B^2}\right). \tag{28}$$

We compute this to be $\beta \approx 0.6$ for the helical ABC cases, $\beta = 0.44$ for the high-helicity spheromak, and $\beta = 0.038$ for the low-helicity spheromak case. However, we have to note that this is the minimum value β attains in our model, since with the presence of magnetic null points within the domain, β is not constant and even diverges at some points. In the external-field cases we have instead $\beta = 20$ (weak field) and $\beta = 1.25$ (strong field).

2.7. Unit Conversions

We choose the conversion rate from code units to physical units such that the dimensions of the setups correspond to physically observed numbers in the intergalactic medium (see Table 2).

Table 1
Simulation Parameters

Model	$\boldsymbol{B}(A_0)$	H_m	ν	η	k/τ	Re	$\mathrm{Re_M}$
hydro	⋯	⋯	10^{-3}	⋯	⋯	960	⋯
hydro2	⋯	⋯	2×10^{-4}	⋯	⋯	4800	⋯
hel_l	0.025	1	10^{-3}	3×10^{-4}	20	1280	4200
hel_h	0.1	4	10^{-3}	3×10^{-4}	5	1280	4200
hel_l2	0.025	1	2×10^{-4}	3×10^{-4}	20	5600	3700
hel_h2	0.1	4	2×10^{-4}	3×10^{-4}	5	6400	4200
sph_l	6.39	1	2×10^{-4}	3×10^{-4}	21.85	7200	4800
sph_h	1.7	4	2×10^{-4}	3×10^{-4}	5.76	11000	7500
ex_low	0.2	0	10^{-3}	3×10^{-4}	⋯	320	1000
ex_high	0.8	0	10^{-3}	3×10^{-4}	⋯	320	1000

Note. The magnetic field intensity, measured by the parameter A_0 in Equation (19), the magnetic helicity H_m, the viscosity ν, the magnetic diffusivity η, the parameter k of the ABC flow in Equation (19) (parameter τ of the spheromak configuration in Equation (21)), the Reynolds number Re and the magnetic Reynolds number $\mathrm{Re_M}$, as defined in Equations (5) and (6).

Table 2
Code Unit Conversion Table

One Code Unit of	Physical Unit
length	10 kpc
time	10 Myr
density	$\times 10^{-25}$ g cm^{-3}
temperature	$\times 10^{6}$ K
magnetic field	$\times 10^{-4}$ G

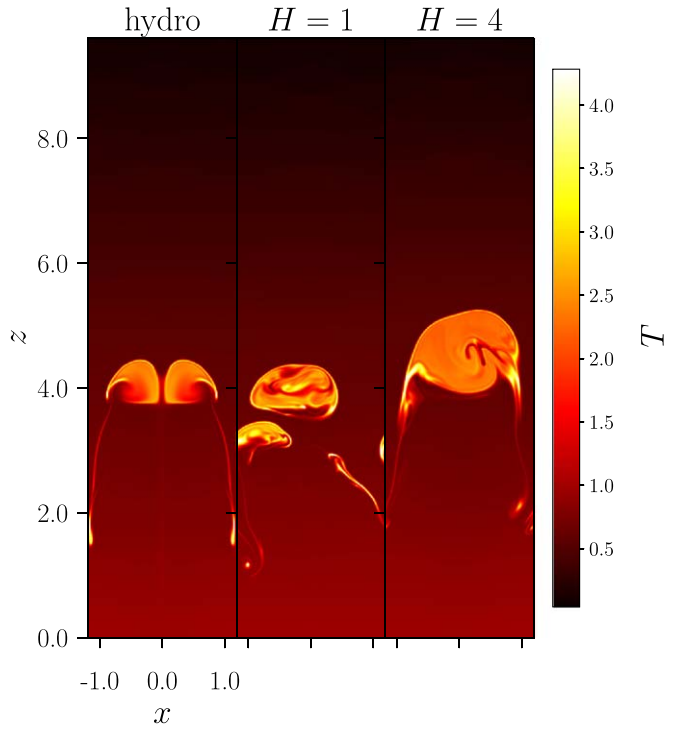

Figure 2. Slices through the simulation domain showing the temperature distribution at final times ($t = 20$) for the purely hydrodynamical case (left), and for the magnetic scenario with the ABC field in the weak-helicity case (center) and strong-helicity case (right). They correspond to models hydro, hel_l, and hel_h in table Table 1.

With these code unit conversions our setup has a size of $L_{xy} = 24$ kpc horizontally and $L_z = 96$ kpc vertically. The cavity has a radius of $r_b = 8$ kpc with a density of $\rho_b = 2.5 \times 10^{-26}$ g cm^{-3} and temperature of $T_b = 4 \times 10^6$ K. The surrounding medium at $z = 0$ has a density of $\rho_0 = 1 \times 10^{-25}$ g cm^{-3} and temperature of $T_0 = 1 \times 10^6$ K. The system experiences a gravitational acceleration of $g = 3.0985 \times 10^{-7}$ cm s^{-2}. Our simulations then run between 200 Myr and 250 Myr. The amplitude of the magnetic field is between $B_0 = 2.5 \times 10^{-6}$ G and $B_0 = 6.39 \times 10^{-4}$ G. For the viscosity we obtain $\nu = 3.0172 \times 10^{27}$ cm^{-2} s^{-1} and resistivity $\eta = 9.0516 \times 10^{26}$ cm^{-2} s^{-1}.

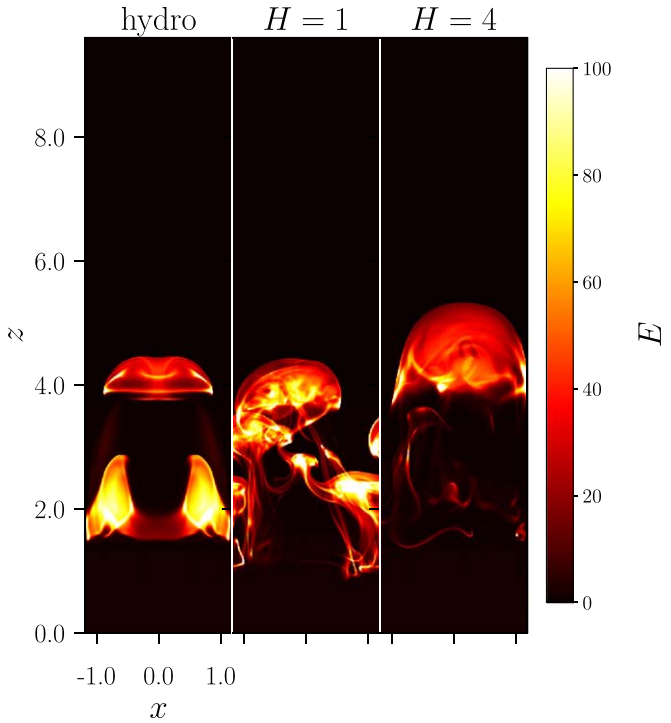

Figure 3. Emission measure at final times ($t = 20$) for the purely hydrodynamical case (left), and for the magnetic scenario with the ABC field in the weak-helicity case (center) and strong-helicity case (right). They correspond to models hydro, hel_l, and hel_h in table Table 1.

3. Effect of an Internal Helical Magnetic Field

3.1. Non-magnetic Test Case

The first case we take into account is the purely hydrodynamical one, to which we will compare the simulations including magnetic fields. As the cavity rises the Kelvin–

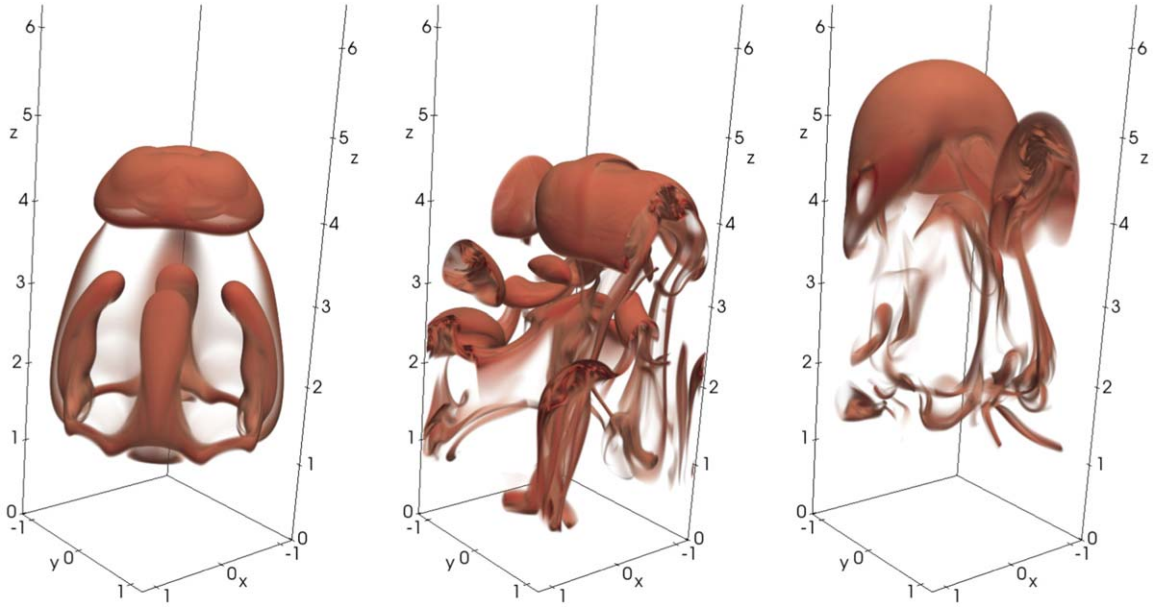

Figure 4. Volume rendering of the temperature of the magnetic cavity for the hydrodynamical case (left), low magnetic helicity (center), and high magnetic helicity (right) at $t = 20$ for the ABC configuration. It is evident that magnetic helicity plays a role in determining the topology of the cavity. In particular, the symmetry seen in the hydrodynamical case is broken when magnetic helicity is non-zero. Note that the four-finger asymmetry in the hydrodynamical case is due to the geometry and finite size of the computational domain.

Helmholtz instability acts on its interface with the surrounding medium and eventually affects the entire cavity by non-linear Kelvin–Helmholtz instability-induced turbulent mixing, as illustrated in the left panels of Figures 2, 3, and 4.

3.2. ABC Configuration

We then perform two different simulations including an ABC helical magnetic field (see Section 2.3) inside the cavity. There it becomes evident that magnetic helicity contributes to keeping the cavity in a significantly more coherent state and prevents its disruption, provided a minimum amount of helicity is present in the field. This is evident from the central and left panels of Figure 2, showing two helical cases: the amount of magnetic helicity in the simulation shown in the right panel is four times larger than that in the central panel.

In order to make it easier to compare our results with observations we create artificial emission measures, assuming an optically thin medium. We place the observer along the y axis at an infinite distance. The emission measure E is then simply the line integral of the temperature to the fourth power,

$$E(x, z) = \int T^4 \, \mathrm{d}y. \tag{29}$$

Similar to the slices plotted in Figure 2, we observe from the emission measures (Figure 3) an increased stability when a helical magnetic field is present.

We can also observe this behavior in the volume rendering of the temperature (Figure 4). While the purely hydrodynamical case (left panel) and the low-helicity case (center) disintegrate after two bubble diameter crossings, the strongly helical case (right) remains largely intact. Furthermore, in the purely hydrodynamical case, the temperature remains symmetric about the central axis of the domain, as expected from symmetry properties of our configuration. This is in agreement with simulations of Ruszkowski et al. (2007), as well as Dong & Stone (2009), who both produced perfectly symmetric configurations in the hydrodynamical case. Conversely, the disruption of the cavity in the low-helicity case develops a very asymmetric, chaotic structure. Also in the high-helicity case, although the disruption is only marginal, we can still observe an asymmetric evolution of the cavity.

To test the stability of the cavities we measure their coherence. In order to do so, we start by defining the space filled by the cavity as the loci for which $\log_{10}(T) > 1.5$. We choose this threshold because the surrounding cold medium has a significantly lower temperature and in the simulated times we do not observe a high enough temperature diffusion or conduction that would reduce the cavity temperature below this value. We then measure the mean distance d_{mean} of all the points in the cavity

$$d_{\mathrm{mean}} = \langle |\boldsymbol{r}_{\mathrm{cavity}} - \boldsymbol{r}_{\mathrm{CM}}| \rangle, \tag{30}$$

where $\boldsymbol{r}_{\mathrm{CM}}$ is the position vector to the center of mass defined as

$$\boldsymbol{r}_{\mathrm{CM}} = \frac{\int_{\log_{10}(T)>1.5} T\boldsymbol{r} \mathrm{d}V}{\int_{\log_{10}(T)>1.5} T \mathrm{d}V}, \tag{31}$$

where $\boldsymbol{r}_{\mathrm{cavity}}$ is the position vector to a point within the cavity, i.e., $\log_{10}(T) > 1.5$, and we take the average over the entire domain. We can therefore study the evolution of d_{mean} with time. Since some of the bubbles rise at different speeds, due to the different magnetohydrodynamic parameters of different models, we can also study the behavior of d_{mean} as a function of the height reached by the bubble, i.e., by its center of mass. For that we also compute the mean height of the bubbles as

$$z_{\mathrm{mean}} = \langle |z_{\mathrm{cavity}} - z_{\mathrm{CM}}| \rangle, \tag{32}$$

where we use the loci for which $\log_{10}(T) > 1.5$, similar to our process for d_{mean}.

Figure 5 (upper panel) depicts d_{mean} as function of z_{mean} in our simulations. We observe that without a magnetic field the cavity is dispersed without extending far from its starting position. An internal magnetic field with low helicity content

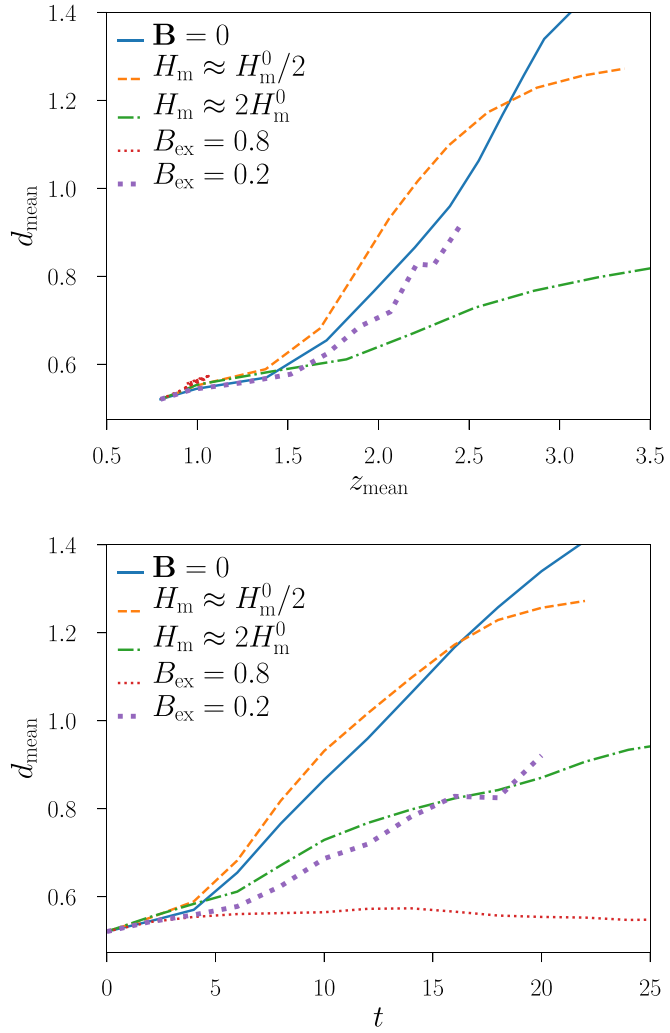

Figure 5. Coherence measure d_{mean} of the cavities as a function of the mean height (upper panel) and time (lower panel) for the hydrodynamical-, weak-, and strong-helicity ABC cases and weak and strong external-field cases. We clearly observe that a large amount of magnetic helicity increases the cavities' stability. A comparable effect can only be obtained with a substantially stronger external magnetic field, but such a field inhibits the ascent of the bubble in the intergalactic medium. The case of a very strong external parallel field keeps the bubble very stable, but it completely obstructs its ascent, thus keeping it confined in the lowest part of the domain. Note that the high-helicity and strong external-field simulations continue well beyond the plotted time limit.

(model hel_l in Table 1) does not improve significantly the stability for almost the whole simulation, but it has a stabilizing effect toward the end. However, an internal field with higher magnetic helicity (model hel_h in Table 1), and the same magnetic energy has some clear positive effect on the bubble's stability. In this latter case we observe a relatively stable rise throughout. Figure 5 (lower panel) depicts instead the time evolution of d_{mean}. Here too it is evident how the strong-helical case is the most stable, while the low helical one only marginally stabilizes the cavity. From Figure 5 we see that high helicity stabilizes the cavity for at least 250 Myr, while the hydrodynamical case and the low-helicity case disrupt after about 100 Myr.

3.3. Behavior at Higher Reynolds Number

We test the effect of a higher fluid Reynolds number on our results by performing simulations with a lower viscosity,

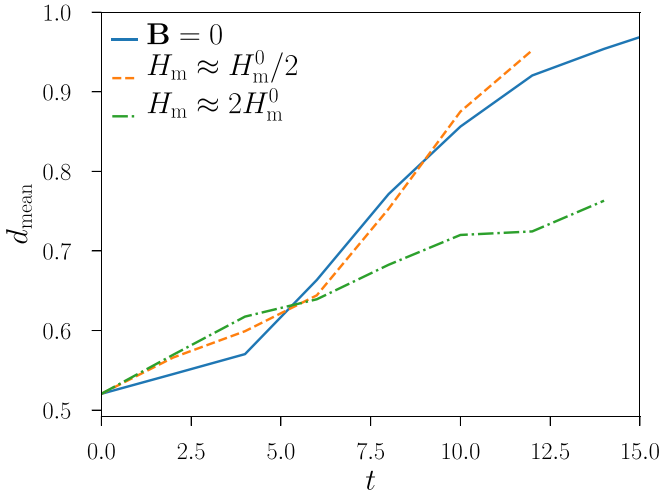

Figure 6. Coherence measure d_{mean} of the cavities for the high-fluid Reynolds number cases as a function of time for the hydrodynamical-, weak-, and strong-helicity ABC cases. The weak-helicity case differs from the the hydrodynamical case in the last part of the simulation. The strong-helicity case shows a clear increase of the bubble stability, confirming our low Reynolds number results.

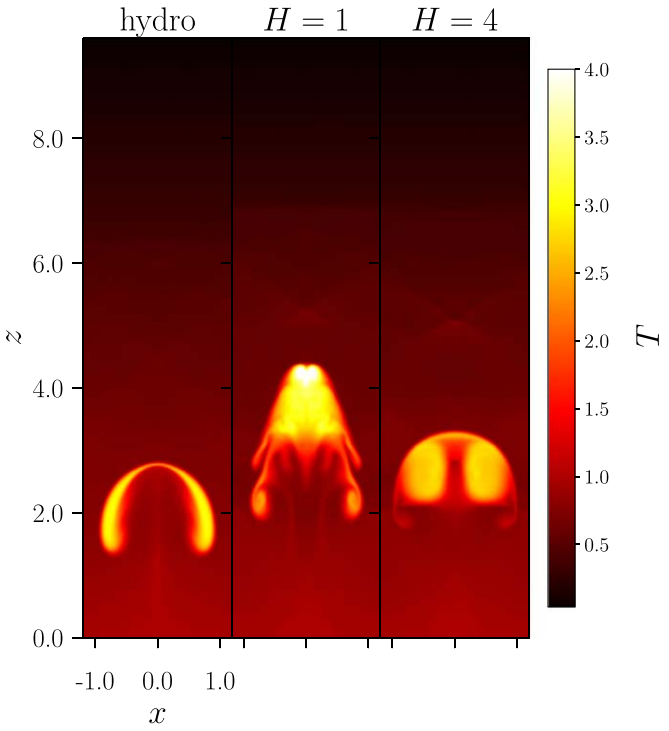

Figure 7. Slices through the simulation domain showing the temperature distribution at times ($t = 8$) for the purely hydrodynamical case (left), weak-helicity spheromak case (center), and strong-helicity spheromak case (right) (models hydro, sph_l, and sph_h in Table 1).

$\nu = 2 \times 10^{-4}$, for the hydrodynamical and the helical cases (models hydro2, hel_l2, and hel_h2 in table Table 1). There we observe a clearer onset of the Kelvin–Helmholtz instability. However, the coherence measure does not change significantly for any of the models compared to the low Reynolds number case, and the relative behavior between the hydrodynamical case and the two cases with internal helical magnetic fields resembles that obtained with higher viscosity (Figure 6).

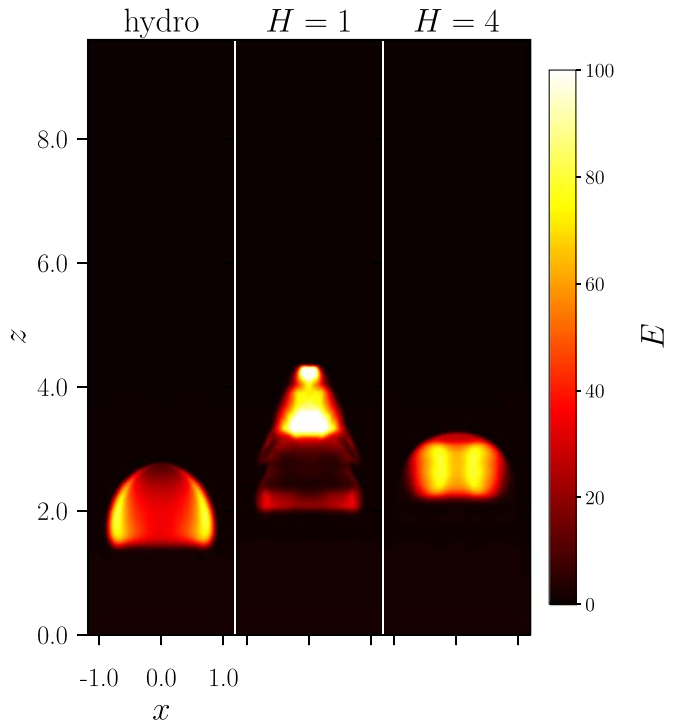

Figure 8. Emission measure at times ($t = 8$) for the purely hydrodynamical case (left), weak-helicity spheromak case (center), and strong-helicity spheromak case (right). They correspond to models hydro, sph_l, and sph_h in table Table 1.

Therefore, this confirms our results in the lower Reynolds number regime.

3.4. Spheromak Configuration

In order to eliminate effects from the particular geometry of the magnetic field, we test the stabilizing properties of the spheromak magnetic field configuration from Equation (21). To obtain a fair comparison with the ABC field case, we want to analyze a scenario with the same amount of magnetic energy and magnetic helicity. To do so, we choose appropriate values for the field amplitude and parameter τ, which in this case plays the same role as the parameter k for the ABC field. Since we have two degrees of freedom we can match both the magnetic energy and the helicity contents, such that our low (high) helicity spheromak configuration has almost the same magnetic energy and helicity as the low (high) helicity ABC configuration (see sph_l and sph_h in Table 1).

From the parameters in Table 1 we can see that our spheromak simulations belong to a high Re and $\mathrm{Re_M}$ scenario. Since the parameters ν and η are the same used in the high Reynolds number cases for the ABC field, we can deduce that higher values of $u_{\max}$ are reached. Due to these localized high velocities of the gas that we attribute to local currents, we are able to run the high-helicity simulation only to a simulation time of ca. 9. Nevertheless, this gives us enough data to confirm the results obtained through the ABC configuration. That is, a high magnetic helicity internal magnetic field can stabilize the bubbles.

We observe this stabilizing effect from the slices of the temperature (Figure 7) and the emission measure (Figure 8). The high-helicity spheromak case clearly stays more stable.

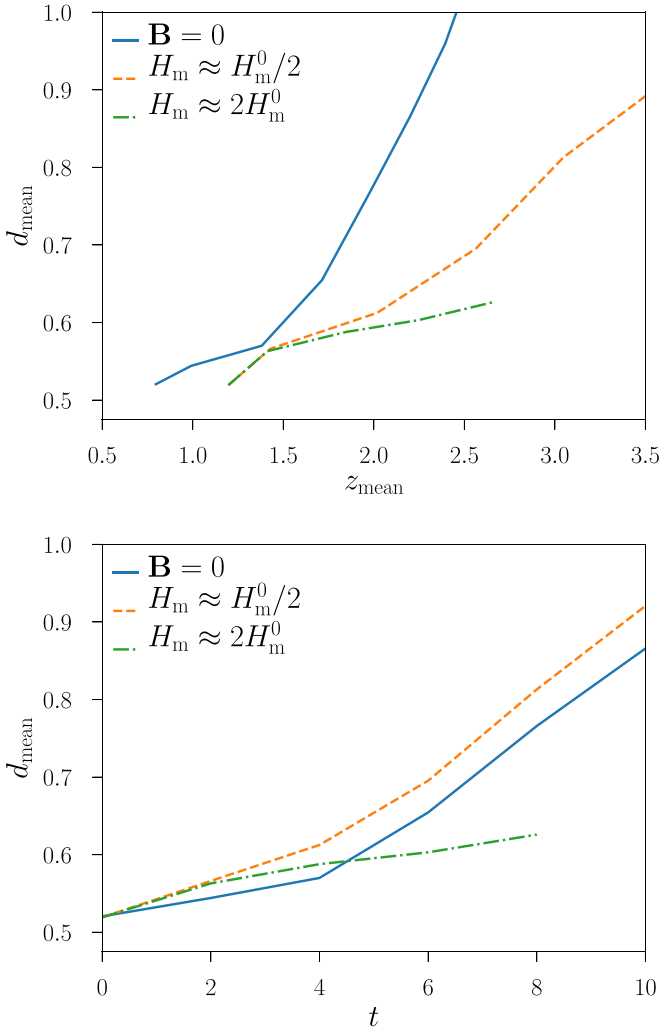

Figure 9. Coherence measure d_mean of the cavities for the high-fluid Reynolds number and hydrodynamical case, and low and high magnetic helicity spheromak cases as a function of mean height (upper panel) and time (lower panel). Although the high-helicity simulation stops at time 9 we can still clearly see that an internal helical magnetic field stabilizes the bubbles and prevents their timely disruption. A small amount of helicity is clearly not sufficient.

From the coherence calculations depicted in Figure 9, where we compare the hydrodynamical case with the low- and high-helicity spheromak cases, this stabilizing effect is evident as well, which is clearly visible in the high-helicity configuration. Conversely, the low-helicity configuration is characterized by a coherence similar to that of the hydrodynamic case. However, from the lower panel of Figure 9 we notice how in the low-helicity case the bubble can reach higher parts of the domain.

4. Effect of an External Parallel Magnetic Field

From Chandrasekhar (1961) and Sharma & Srivastava (1968) we know that the Kelvin–Helmholtz instability is suppressed by a magnetic field that is aligned (parallel) to the velocity. Comparing Equation (13) in chapter IV from Chandrasekhar (1961) with our induction Equation (1) we observe that we can identify our $\boldsymbol{B}$ with $\boldsymbol{H}$ and the magnetic resistivity η has the same definition and permeability $\mu = 1$ in our formulation.

With that we can write equation (205) in chapter XI from Chandrasekhar (1961) as

$$B^2 \geqslant 2\pi(u_1 - u_2)^2(\rho_1\rho_2)/(\rho_1 + \rho_2), \quad (33)$$

which gives us a criterion for the Kelvin–Helmholtz instability to be entirely suppressed for a two-layer system with densities ρ_1 and ρ_2 and velocities u_1 and u_2. For our hydrodynamic simulations we observe a velocity difference of ca. 0.5, while our densities are 1 (surrounding medium) and 0.25 (hot cavity). We estimate the magnetic field strength parallel to the velocity to be ca. 0.56 for suppressing the Kelvin–Helmholtz instability.

Here we present the evolution of a cavity with $\boldsymbol{B} = 0.8\boldsymbol{e}_z$ and one with $\boldsymbol{B} = 0.2\boldsymbol{e}_z$. That is, one will exhibit Kelvin–Helmholtz suppression at all scales, while the other will not. For a field that is strong enough for suppression we are in a situation with little buoyancy, that is z_{mean} remains approximately constant in time (Figure 5). Note that both cases with a magnetic field along $\boldsymbol{e}_z$ have a total magnetic energy between one and two orders of magnitude higher than the helical cases.

5. Discussion and Conclusions

In this work we have examined the possibility that a helical magnetic field may play a key role in the stability of extragalactic bubbles, similar to the Fermi bubbles observed rising from the midplane of our Galaxy in the intergalactic medium. This hypothesis appears justified, because these bubbles are thought to be inflated by AGN or from jets coming from the galactic center. Such jets have been observed to be characterized by helical magnetic fields, which is a consequence of the rotation of strong magnetic field from their sources. Since magnetic helicity is conserved in a high-conductivity medium such as the intergalactic medium, it is reasonable to expect the bubbles rising in the intergalactic medium to retain their helical magnetic field. As we used parameters that can be compared to measurements from the intergalactic medium, we can directly compare our simulations and observations.

For the purely hydrodynamical case we observe a longer stability (ca. 80 Myr) than has been predicted for bubbles in the intergalactic medium, although with an increase of ca. 50% in the coherence measure d_{mean}. While a parallel magnetic field is known to suppress the Kelvin–Helmholtz instability, for intergalactic magnetic cavities the field strength would need to be rather large. Here we have shown that we can exploit the stability properties of magnetically helical structures to keep these cavities from disrupting, with a much smaller magnetic energy content.

We used a general helical magnetic field in the form of the ABC flow that fills a bubble rising through buoyancy in an otherwise stably stratified medium. We quantify the disruption of the bubble by measuring the parameter d_{mean}, the mean distance of all the points contained in it. We observed that this bubble is stabilized and does not develop a Kelvin–Helmholtz instability in the interface with the surrounding medium if the magnetic field is sufficiently helical. We estimated that a helical field with maximum strength of the order of 10^{-5} G can stabilize the bubble over a timescale of about 250 Myr. Here we see that during that time the high-helicity case never exceeded a value of d_{mean} twice its initial value. Conversely, a less helical magnetic field, with a total magnetic helicity four times lower, could not keep the bubble stable and this case exhibits a disruption similar to that for the non-magnetic case. In the low-helicity and hydrodynamic cases d_{mean} increases by more than twice its initial value.

To verify that our results do not depend on a specific initial geometry, we performed additional simulations using a different initial magnetic field filling the bubble. We used a spheromak field with the same initial magnetic energy and helicity content. By evaluating the coherence measure of the bubble we showed how the overall evolution of the system is similar to that of the ABC cases, thus showing the important role played by magnetic helicity.

Therefore, based on the results presented here, we propose that an internal helical magnetic field is a viable explanation for intergalactic bubble stability, requiring only relatively low magnetic energies compared to the external magnetic field hypothesis.

The authors appreciate the support given by the HPC3 Europe program HPC-EUROPA3 (INFRAIA-2016-1-730897). S.C. acknowledges financial support from the UK's STFC (grant number ST/K000993). For the plots we made use of the Matplotlib library for Python (Hunter 2007) and BlenDaViz.[6] The authors thank the Department of Physics of the University of Crete for the hospitality and Evangelia Ntormousi, Alexander Russell, David I. Pontin, Gunnar Hornig, and Ross Palister for constructive and critical discussions. We thank the anonymous referee for the constructive critique that led to substantial improvements of this paper.

ORCID iDs

Simon Candelaresi https://orcid.org/0000-0002-7666-8504

References

Aly, J.-J., & Amari, T. 2012, MNRAS, 420, 237
Bîrzan, L., Rafferty, D. A., McNamara, B. R., Wise, M. W., & Nulsen, P. E. J. 2004, ApJ, 607, 800
Braithwaite, J. 2010, MNRAS, 406, 705
Brüggen, M. 2003, ApJ, 592, 839
Candelaresi, S., & Brandenburg, A. 2011, PhRvE, 84, 016406
Carilli, C. L., Perley, R. A., & Harris, D. E. 1994, MNRAS, 270, 173
Carilli, C. L., & Taylor, G. B. 2002, ARA&A, 40, 319
Chandrasekhar, S. 1961, Hydrodynamic and Hydromagnetic Stability (Oxford: Oxford Univ. Press)
Churazov, E., Brüggen, M., Kaiser, C. R., Bohringer, H., & Forman, W. 2001, ApJ, 554, 261
Del Sordo, F., Candelaresi, S., & Brandenburg, A. 2010, PhRvE, 81, 036401
Dong, R., & Stone, J. M. 2009, ApJ, 704, 1309
Gabuzda, D. 2018, Galax, 7, 5
Gourgouliatos, K. N., Braithwaite, J., & Lyutikov, M. 2010, MNRAS, 409, 1660
Hunter, J. D. 2007, CSE, 9, 90
Jones, T. W., & De Young, D. S. 2005, ApJ, 624, 586
Li, H., Lapenta, G., Finn, J. M., Li, S., & Colgate, S. A. 2006, ApJ, 643, 92
Liu, W., Hsu, S. C., Li, H., Li, S., & Lynn, A. G. 2008, PhPl, 15, 072905
McNamara, B., & Nulsen, P. 2007, ARA&A, 45, 117
Montmerle, T. 2011, in EAS Publ. Ser. 51, Star Formation in the Local Universe, ed. C. Charbonnel & T. Montmerle (Les Ulis: EDP Sciences), 299
Pizzolato, F., & Soker, N. 2006, MNRAS, 371, 1835
Robinson, K., et al. 2004, ApJ, 601, 621
Ruszkowski, M., Enßlin, T. A., Brüggen, M., Heinz, S., & Pfrommer, C. 2007, MNRAS, 378, 662
Sharma, R. C., & Srivastava, K. M. 1968, AuJPh, 21, 917
Sternberg, A., & Soker, N. 2008, MNRAS, 389, L13
Su, M., Slatyer, T. R., & Finkbeiner, D. P. 2010, ApJ, 724, 1044
Tang, X. Z. 2008, ApJ, 679, 1000
Taylor, G. B., Fabian, A. C., & Allen, S. W. 2002, MNRAS, 334, 769
Vogt, C., & Enßlin, T. A. 2005, A&A, 434, 67
Yang, H.-Y., Ruszkowski, M., & Zweibel, E. 2018, Galax, 6, 29

[6] https://github.com/SimonCan/BlenDaViz